Coseismic and postseismic displacements from the 1978 M_w 7.3 Tabas-e-Golshan earthquake in eastern Iran

Yu Zhou[a,*], Richard T. Walker[a], James Hollingsworth[b,c], Morteza Talebian[d], Xiaogang Song[e], Barry Parsons[a]

[a] *COMET, Department of Earth Sciences, University of Oxford, Oxford OX1 3AN, UK.*
[b] *Université Grenoble Alpes, ISTerre, 38058 Grenoble, France.*
[c] *CNRS, ISTerre, UMR 5275, 38058 Grenoble, France.*
[d] *Research Institute for Earth Sciences, Geological Survey of Iran, Azadi Square, Meraj Blvd, Tehran, Iran.*
[e] *State Key Laboratory of Earthquake Dynamics, Institute of Geology, China Earthquake Administration, Beijing 100029, China.*

Abstract

We use optical image correlation of historical aerial photographs, and modern satellite images to investigate the 1978 M_w 7.3 Tabas-e-Golshan thrust earthquake in eastern Iran. Correlation of images between 1974 and 1991 reveals a near-surface shortening component of ∼2.9 m across the margin of the Tabas fold, which is a combination of coseismic and postseismic deformation. Correlation of images between 1991 and 2013 shows a further ∼0.3 m of postseismic shortening. Using six pre-earthquake aerial photographs acquired in 1956 and stereo SPOT-6 imagery from 2013, we also generate pre- and post-earthquake digital elevation models (DEMs) for one of the main fold segments. Differencing of the two DEMs reveals a height change of ∼4.7 m. Elastic dislocation modelling of the 1974–2013 displacement field requires 7 m slip on a 50° dipping fault, extending from a depth of 0.1 km to 6 km at

*Corresponding author.
Email address: yu.zhou@earth.ox.ac.uk (Yu Zhou)

July 19, 2016

its base (the majority of slip, ∼6.5 m, occurred prior to 1991). Our results, combined with previous InSAR observations, indicate time-decaying shallow postseismic afterslip. It is likely that most of the afterslip occurred prior to 1991. The slip appears to dissipate in the near surface, and is accommodated as a narrow band of flexural slip on bedding planes. Comparison of the fault slip model with terrace heights measured from the SPOT-6 DEM suggests that the Tabas fold system may exhibit characteristic slip behaviour. Such behaviour would require a magnitude M_w 7.3 earthquake every ∼3500 years, based on the previously estimated shortening rate of ∼1.0 mm/yr. This study highlights the usefulness of historical imagery in investigating past earthquakes, thus providing new information about historical faulting in continental regions.

Keywords: 1978 Tabas earthquake, Historical optical imagery, Afterslip, Characteristic slip behaviour, Continental tectonics, Seismic hazard

1. Introduction

Measurements of surface deformation in earthquakes and by postseismic creep reveal how active folds and faults evolve over the seismic cycle (*Burbank and Anderson*, 2011, *Copley*, 2014, *Dolan et al.*, 2003, *Yu et al.*, 2003). They provide the most valuable source of data for the accurate description and understanding of continental tectonics, and for investigating present and future seismic hazard (*Berberian*, 1981, *Hubbard and Shaw*, 2009, *Molnar and Lyon-Caen*, 1989, *Molnar et al.*, 1973, *Tapponnier et al.*, 1990). Large continental earthquakes ($M_w \geq 7$) often occur on faults that were previously unmapped or poorly studied, due to the long recurrence times between events and their subtle geomorphological expression in the landscape (*England and Jackson*, 2011, *Fialko et al.*, 2005, *Funning et al.*, 2005, *Jackson*, 2001, *Oskin et al.*, 2012, *Zhang*, 2013, *Zhou et al.*, 2015a). Large blind thrust earthquakes, e.g. the 2015 Gorkha earthquake in Nepal (*Elliott et al.*, 2016, *Feng et al.*, 2015, *Grandin et al.*, 2015, *Wang and Fialko*, 2015), have been uncommon in the era of modern satellite geodesy. Due to their hazardous nature, there is a strong need to re-examine older events to improve our understanding of the factors controlling the rupture of blind thrust faults.

The September 16, 1978 M_w 7.3 Tabas-e-Golshan earthquake in eastern Iran (hereafter referred to as the Tabas earthquake) is an example that occurred prior to the onset of interferometric synthetic aperture radar (InSAR) and Global Positioning System (GPS) monitoring, rupturing a series of previously unrecognised blind thrust faults. It is the only known large event in

the epicentral area for at least the last 1,000 years, and completely demolished the oasis town of Tabas, killing ∼11,000 people, 85% of its population (*Berberian*, 1979, *Berberian et al.*, 1979, *Walker et al.*, 2003, 2013).

Berberian (1979) mapped 85 km of discontinuous surface ruptures 10 days after the 1978 earthquake. Much of the surface faulting took the form of small amounts of slip on multiple bedding planes, suggesting that much of the slip at depth failed to reach the surface and was instead accommodated as flexural-slip folding. The maximum coseismic vertical displacement localised on the main frontal thrust fault on the segment south of Tabas was measured to be ∼35 cm, but adjacent bedding slip totalled ∼150 cm (*Berberian*, 1979). Because most of the coseismic slip was concentrated at depth (*Berberian*, 1982, *Walker et al.*, 2003), it is not possible to determine the pattern and magnitude of seismogenic slip and the sub-surface structure from mapping of discrete surface ruptures alone. Geodetic measurements of coseismic and postseismic displacement are unavailable, since GPS and InSAR monitoring were not available at the time of the 1978 Tabas earthquake. Nevertheless, *Copley* (2014) used InSAR to image shallow creep on the fold ∼6 km S-E of the town of Tabas (hereafter referred to as the Tabas fold) 30 years after the event.

The declassification of US Hexagon Keyhole-9 imagery (hereafter referred to as KH-9) allows us to investigate historical earthquakes back to the early 1970s (*Burnett*, 2012, *Hollingsworth et al.*, 2012) as they provide a visual record of the landscape prior to the earthquake. In this study, we use sub-

pixel optical image correlation to retrieve the coseismic and postseismic deformation fields. We first correlate KH-9 images acquired in 1974 with SPOT-2 satellite images acquired in 1991, and also modern high-resolution SPOT-6 data, to determine the horizontal displacements associated with the 1978 Tabas earthquake, from which we invert for the fault structure and earthquake slip. We also use six pre-earthquake aerial photographs acquired in 1956 and a post-earthquake SPOT-6 stereo data set acquired in 2013 to generate the pre- and post-earthquake topography respectively for one of the main fold segments (the same one as *Copley* (2014)). By differencing the pre- and post-earthquake topography, we measure the coseismic and postseismic height changes which allow us to better constrain the fault slip model. By reconciling our best-fit fault slip model with analysis of the long-term surface folding observed in the SPOT-6 topography, we constrain the 3D evolution of active thrust faulting in this region throughout the Late Quaternary.

2. Tectonic background of the 1978 Tabas earthquake

Iran is actively deforming in response to the collision of Arabia with Eurasia at a rate of ∼25 mm/yr at longitude 60° (*Vernant et al.*, 2004a, *Walker and Jackson*, 2004). Regional deformation is characterised by distributed folding, reverse faulting, and strike-slip faulting (*Berberian*, 1981, *Jackson et al.*, 1995, *Walker and Jackson*, 2004) (Figure 1a). Studies based on plate models and GPS measurements indicate that up to half of the total Arabia-Eurasia shortening is taken up by north-south shortening in the

Zagros mountains of southwestern Iran (∼10-15 mm/yr) (*Hessami*, 2002, *Jackson et al.*, 1995, *Tatar et al.*, 2002, *Walpersdorf et al.*, 2006) with the Alborz accommodating a further 5±2 mm/yr north-south shortening (*Vernant et al.*, 2004b) and subduction of the South Caspian for another ∼5–10 mm/yr (*Hollingsworth et al.*, 2008). The northward motion of central Iran relative to western Afghanistan results in ∼15 mm/yr north-south right-lateral shear (*Mousavi et al.*, 2013, *Walker and Jackson*, 2004, *Walpersdorf et al.*, 2014), accommodated across several right-lateral strike-slip faults bordering the Dasht-e-Lut Desert in eastern Iran. These include the East Neh (1.75-2.5 mm/yr from *Meyer and Le Dortz* 2007), West Neh (1-5 mm/yr from *Meyer and Le Dortz* 2007) and Zahedan faults in the east, and the Sabzevaran (∼6 mm/yr from *Regard et al.* 2006), Gowk (∼3.8–5.7 mm/yr from *Fattahi et al.* 2014, *Walker et al.* 2013) and Nayband (∼1.4 mm/yr from *Walker et al.* 2009 and ∼1.8 mm/yr from *Foroutan et al.* 2014) segments in the west (Figure 1a). The 1978 Tabas earthquake occurred at the northern end of the Nayband fault where north-south right-lateral strike-slip motion turns into a zone of distributed thrusting that is manifest at the surface as a series of folds within Neogene basin deposits.

The Tabas region had been quiescent for at least 1,100 years until the 1978 earthquake (*Berberian*, 1979). Detailed field mapping 10 days after the earthquake (*Berberian*, 1979) revealed extensive slip on folded Neogene bedding planes along the 85 km-long system of folds, and some high-angle faults within the folds that are likely tensional features (Figure 2), consistent

with coseismic fold growth (e.g. *Walker et al.* 2003). *Berberian* (1979) also measured a maximum displacement of ∼35 cm along a discrete east-dipping reverse fault at the western margin of the Kurit fold segment (Figure 2). Assuming a single, simple rupture event, *Walker et al.* (2003) estimated an average slip of ∼3.3 m using a rupture velocity of ∼3.5 km/s, main shock source time function duration of 18 s, and typical ratio of average slip to rupture length ($\overline{\mu}/L$) of 5×10^{-5} (*Scholz*, 1982). The relatively small surface slip measured in the field (∼35 cm) implies that most of the coseismic slip at depth failed to reach the surface (*Walker et al.*, 2003). The source parameters of the main shock indicate slip on a detachment thrust fault dipping ∼16°E with a centroid depth of ∼9 km and with an epicentre southeast of the folding (*Walker et al.*, 2003, 2013). Analysis of 329 aftershocks shows a concentration of events around depths of 5-10 km (*Berberian et al.*, 1979). *Copley* (2014) estimated ∼5 mm/yr postseismic afterslip on a steep ramp beneath the Tabas fold, extending to a depth of 4-5 km, from modelling InSAR observations in the interval 1996–1999 (Figure 2). By combining all the available information, and assuming that postseismic afterslip decays with time rapidly (*Segall et al.*, 2000), *Copley* (2014) inferred that the majority of the slip gradient was relaxed aseismically prior to 1996 by postseismic motion on a high-angle thrust ramp that connects the surface anticlines to the coseismic low-angle detachment fault at depth.

3. Image processing

To measure the surface displacement associated with the 1978 Tabas earthquake, we first obtained a KH-9 image acquired in 1974, six aerial photographs taken in 1956, a SPOT-2 image from 1991 and a SPOT-6 stereo data set from 2013 (listed in Table 1). Correlation of the KH-9 and SPOT-2 imagery provides information about the coseismic and relatively early postseismic horizontal motion, whereas the SPOT-2 and SPOT-6 imagery can be used to measure the horizontal motion in the later postseismic period. All correlations include some component of postseismic motion as the earliest post-earthquake imagery we use was acquired 13 years after the main shock.

Furthermore, we use the aerial photographs to generate a pre-earthquake digital elevation model (DEM) from 1956 and the stereo SPOT-6 imagery to generate a post-earthquake DEM from 2013. By differencing the two DEMs, we can also measure the height changes between 1956 and 2013. In this section, we describe the methods of processing these various images.

3.1. SPOT-6 images obtained in 2013

The SPOT-6 satellite was launched on the 9th September 2012, in a sun-synchronous orbit with a repeat cycle of 26 days (*Astrium*, 2013). It can provide 1.5 m resolution panchromatic and 6 m resolution multispectral images over a swath footprint of 60 km for high-resolution stereo mapping (*Astrium*, 2013). We purchased one tri-stereo data set tasked on the 29th December 2013 over an area of 918 km^2 (Figure 1b). Provided with the

rational function models of the three SPOT-6 images, we processed the data using the Leica Photogrammetry Suite (LPS) with a pairwise pixel-by-pixel matching procedure (see Supplementary Material for details) (*Zhou et al.*, 2015b). The point cloud extracted from the new automatic terrain extraction module (eATE) in LPS was filtered by averaging within a cell of 2 m and then gridded with a pixel spacing of 2 m (coordinate system: WGS84 UTM 40N). The SPOT-6 image was then orthorectified using the 2 m DEM. The SPOT-6 orthoimage (Figure 2b) is used as the reference image for co-registration of all earlier imagery in the following sections.

3.2. KH-9 image obtained in 1974

The KH-9 mapping program consisted of 12 missions (mission numbers: 1205-1216) (*Burnett*, 2012). The first mission (1205) was operational from the 9th March 1973 to the 20th April 1973, with a duration of 42 days (*Burnett*, 2012). Many subsequent missions followed, before the program ended on the 14th October 1980, having amassed a total of ∼29000 images with a resolution of 6-9 m globally. Each KH-9 image has a footprint of 125 km × 250 km, and is available for purchase from the USGS EarthExplorer website for $30. However, detailed information about the camera system used for earth mission, such as focal length, optical distortions and film size is unavailable. It has been concluded from different experiments that KH-9 uses a camera similar to the NASA Large Format Camera (LFC), a 23×46 cm frame camera with a focal length of 30.5 cm (*Hollingsworth et al.*, 2012,

Mollberg and Schardt, 1988, *Surazakov and Aizen*, 2010).

Figure 1b shows a KH-9 image covering the Tabas region, acquired on the 26th November 1974 (mission 1209). No post-earthquake KH-9 imagery is available for the Tabas region. The KH-9 image was processed using the aerial photo module of COSI-Corr (*Ayoub et al.*, 2009). We first used a bilinear interpolation to resample the SPOT-6 orthoimage to 6 m to match the lower resolution KH-9 image. The KH-9 image was then co-registered to the 6 m SPOT-6 orthoimage using 7 ground control points (GCPs) collected 10-20 km from the Tabas fold, where the maximum surface displacement was observed in the field (*Berberian*, 1979) and the postseismic interferograms (*Copley*, 2014). In the absence of a suitable pre-earthquake DEM, the KH-9 image was orthorectified using the post-earthquake SPOT-6 DEM (the DEM generated from the pre-earthquake aerial photographs contains large errors due to tilting and various distortions including scanning, optical and film distortions, discussed in Section 4.2). As a result, any height changes will cause an apparent horizontal signal (discussed in *Hollingsworth et al.* (2012) and *Barišin et al.* (2015)). In our case, this influence ($\leq$0.5 m) is insignificant compared to the tectonic signal ($\sim$3.5 m) because the location of the Tabas fold within the KH-9 image is close to the centre, as discussed in Supplementary Material.

3.3. SPOT-2 in 1991

The SPOT-2 satellite was launched on the 22nd January 1990, and de-orbited in July 2009. The products, including 10 m resolution panchromatic and 20 m resolution multispectral images, were acquired over a swath footprint of 60 km. Figure 1b shows the coverage (1000 km^2) of the SPOT-2 panchromatic image that we purchased for this study. It was acquired on the 6th September 1991 with an incidence angle of -2.2°. Following the same procedure as described in Section 3.2, we co-registered the SPOT-2 image to the SPOT-6 orthoimage using 6 GCPs (as shown in Figure 1b) and orthorectified it using the SPOT-6 DEM.

3.4. Aerial photographs obtained in 1956

Six aerial photographs covering the Tabas region were acquired on the 13th August, 1956, as part of a country-wide survey. The aerial photographs were scanned from print copies at a resolution of 1200 dpi × 1200 dpi using an EPSON Expression 11000XL scanner. We orthorectified the aerial photographs using a frame camera model in LPS to generate a pre-earthquake DEM. Interior orientation parameters consist of the focal length and the location of the principal point. The focal length (155.24 mm) is provided with the photograph, and the location of the principal point was estimated using the fiducial points on the four edges of each image. The exterior orientation parameters (the location, elevation, and three rotation angles of the camera) were estimated with a least-squares adjustment using 36 GCPs

identified from the SPOT-6 imagery and DEM, along with 108 tie points (points whose ground coordinates are unknown, but are common to both images). After having solved the orientation parameters for all aerial photographs, we extracted a DEM (5 m spatial resolution) with eATE in LPS (see Supplementary Material for the aerial DEM).

4. Results

4.1. Horizontal displacement from image correlation

We estimated horizontal displacements by correlating the KH-9 (resampled to 6 m), SPOT-2 (resampled to 6 m) and SPOT-6 (resampled to 6 m) images in COSI-Corr (*Leprince et al.*, 2007). A multi-scale correlation window of 64 pixels was used, followed by 32 pixels, with a step of 8 pixels (48 m) (*Ayoub et al.*, 2009). COSI-Corr can measure surface displacements with subpixel precision (*Hollingsworth et al.*, 2012, *Leprince et al.*, 2007, *Zhou et al.*, 2015b). We also tested different parameters in the correlation procedure (see Figure S2 in Supplementary Material), and the results from alternative correlation window sizes (32×32 pixels or larger) all show a similar dislocation pattern, increasing our confidence in the validity of the results.

In this study, we focused on the north-south striking Tabas fold for three reasons: (1) although the N-S displacement field was heavily contaminated by the scanning artifacts (see Figure S1 in Supplementary Material), the E-W displacement field, which contains all of the tectonic signal, is free from such contamination; (2) it is located in the centre of the image, where the

incidence angle is close to nadir, thereby minimising topographic residuals which can contaminate the horizontal displacement fields (see Supplementary Material); (3) we have constraints on the fold structure from inversion of postseismic InSAR.

Figures 3a, 4a and 4d show the E-W displacement fields across the Tabas fold over different time intervals. In general, the relatively old alluvial materials within the fold and the minimal vegetation cover result in high coherence in the correlations even 35 years after the earthquake. Despite the longer time interval, the correlation result from the high-resolution imagery (SPOT-6) (Figure 3a) is much less noisy than that from the lower-resolution imagery (SPOT-2) (Figure 4a). To determine the displacement, we projected all the measurements onto the fault-perpendicular direction (line AB in Figure 3a), and averaged the data in 50 m wide bins to increase the signal-to-noise ratio. By doing so, we obtained a displacement profile for each correlation result. There are some large localised westward displacements (negative values) over agricultural areas, which appears to be caused by subsidence due to water pumping (see Section 3 in Supplementary Material), so we masked out those areas and only used the data points included in the dashed polygon. From the displacement profile in Figure 3b, we found an E-W offset of 3.4±0.3 m (i.e. shortening) from 1974 to 2013. Most of the displacement (2.9±0.2 m) occurred over the interval 1974-1991 (Figure 4b), with a small amount (0.3±0.1 m) over the interval 1991-2013 (Figure 4e). These displacement profiles are used to determine the fault geometry and slip at depth in Section 5.1.

4.2. Height changes from DEM differencing

By differencing the pre-earthquake DEM generated from the aerial photographs and the post-earthquake SPOT-6 DEM, we also measured the height changes between 1956 and 2013. The elevation differences in Figure 5a show warping at the edge of each aerial photograph which covers part of the mosaic. These are non-tectonic signals in the pre-earthquake DEM, caused by the strong radial distortions at the edge of the images, problems with matching pixels with large differences in incidence angles in these areas, and film distortions (e.g. bending) due to duplication and storage over almost six decades. The resulting elevation errors in the pre-earthquake DEM can be as large as several metres, so we did not use the aerial photographs and the DEM for image matching. Also, we did not account for the horizontal motion in DEM differencing because (1) we cannot solve the horizontal displacements between the two DEMs, and (2) the area is relatively flat with a regional slope of $\leq 2^{\circ}$ (see the topographic profiles in Figure 9b), which means that the horizontal displacements would not cause large apparent vertical motion.

Despite the large long-wavelength film distortions in Figure 5a, we can still measure the shorter-wavelength dislocation at the fold front. We projected the elevation differences in the area where we measured the horizontal displacements onto the fault-perpendicular direction (line SS$'$ in Figure 5a). Profile SS$'$ in Figure 5b shows a height change of $\sim$4.7 m at the fault over the interval 1956-2013.

5. Discussion

5.1. Models of fault slip

Based on the earthquake surface deformations, we are able to model the fault geometry and slip at depth, using an elastic dislocation approach (*Okada*, 1985). For the modelling, we assume constant slip on a rectangular plane to estimate the geometry and slip of the faulting. As the KH-9 and SPOT-6 correlations have good coherence (Figure 3), we use this result for determining the fault model. We varied the depth to the top of the fault plane from 0-0.5 km in steps of 0.1 km, the depth to the bottom from 4-10 km in steps of 1 km, the dip from 40-80° in steps of 5° and fault slip from 3-9 m in steps of 0.5 m. The strike and rake were fixed to 2° and 90° (i.e. pure thrust motion). We then performed a grid search to find the best fit to our measurement. Because we do not have any reference point in the displacement field, a linear trend is evident in the measured profile (Figure 3b). We computed the residuals between each Okada model and the measured profile, and fitted a linear trend based on the residuals. We then removed the linear trend from the measured profile, and recalculated the residuals between the predicted displacement and the new profile. As the data is noisy, we are limited in what we can resolve in the modelling. The solution with minimum misfit (the standard deviation of the residuals) gave 7±0.5 m slip on a 50±5° dipping fault, from a depth of 0.1 km to 6±1 km at its base (Figure 3c). We give examples of the fits of other models in Supplementary Material. This fault geometry is consistent with that obtained by modelling the postseismic

deformation observed using InSAR (*Copley*, 2014), i.e. a dip of 55±10° and bottom depth of ∼4–5 km. Note that *Copley* (2014) modelled surface slip, i.e. a top depth of 0 km, but this model does not fit the displacement from image correlation, as shown in Figure S4 in Supplementary Material. Our model with a top depth of 0.1 km is more consistent with the measurement, which suggests that the main fault slip did not reach the surface.

We also calculated the theoretical height change, and compared it to the measurement from DEM differencing. As explained in Section 4.2, the mismatch between the modelled height change and profile SS′ is caused by a combination of a lack of reference points and film distortions in the aerial photographs. We modelled the distortion function as a third-order polynomial (*Brown*, 1971) and calculated the coefficients of the polynomial based on the residuals between the Okada model and the measured profile. The polynomial was removed from profile SS′ (Figure 5c). Similarly, we performed a grid search procedure and obtained 7 m slip on a 50–60° dipping fault, from a depth of 0.1 km to ∼5–7 km at its base (Figure 5c), providing an additional constraint on the fault slip model.

As the KH-9 and SPOT-2, and SPOT-2 and SPOT-6 correlations are much noisier, we did not use them to model the fault geometry. Instead, we used the best-fitting fault geometry obtained from the KH-9 and SPOT-6 correlations (a fault plane with a strike and dip of 2°/50°, from a depth of 0.1 km to 6 km at its base), and repeated the modelling procedure (*Okada*, 1985) to determine the total slip in the intervals 1974-1991 and 1991-2013

by varying the magnitude of slip in steps of 0.25 m. Similarly, a linear trend was fitted based on the residuals between the prediction and the displacement profile, and removed from the displacement profile before comparing the models and the measurement, i.e. inverting for the linear ramp, as well as the slip values. Based on the minimum misfit, we found 6.5 m slip in the coseismic and early postseismic periods (1974-1991) (Figure 4c), and 0.5 m slip in the late postseismic period (1991-2013) (Figure 4f).

Walker et al. (2003) and *Copley* (2014) suggested that the 50° dipping fault beneath the Tabas fold is connected to a low-angle (16°) fault at depth (the subsurface structure is discussed in Section 5.3). We also tested how much of the slip that we retrieve across the Tabas fold could result from slip on the low-angle fault at depth. We assumed a slip of ∼3.3 m on a 16° dipping fault from a depth of 6 km to 9 km at its base (*Walker et al.*, 2003), and calculated the surface displacements across the Tabas fold. Any surface signal from a fault dipping at 16° at depths of 6–9 km will produce a very long-wavelength signal, which we are insensitive to. However, it does not produce a short-wavelength signal. As shown in Figure S5 in Supplementary Material, both the horizontal and vertical displacements produced by slip on the low-angle fault at depth are very small (less than 5 cm). It is therefore reasonable to assume that the deformation signal measured in our study is purely due to slip on the 50° dipping fault in the inversions.

5.2. Timescale of the deformation

Copley (2014) and this study have both observed long-lasting shallow afterslip, which has continued for more than 30 years following the 1978 Tabas earthquake. Similar observations have been made for other earthquakes, e.g. afterslip continued for at least 40 years following the 1964 Alaska earthquake (*Suito and Freymueller*, 2009) and 12 years after the 1999 Izmit earthquake (*Çakir et al.*, 2012). Afterslip has also been suggested to markedly decay with time (*Segall et al.*, 2000). In the case of the 1978 Tabas earthquake, *Copley* (2014) discussed the features of the postseismic motion in detail based on the InSAR observations from 1996 to 2010, and speculated that most of the postseismic deformation should have occurred prior to 1996, assuming a time-decaying rate (which was also observed from the difference between the ERS data in 1996–1999 and the Envisat data in 2003–2010). Since our observations cover an earlier period, we provide additional information about the timescale of the Tabas postseismic deformation.

Observations of laboratory experiments and many natural earthquakes have suggested that postseismic deformation following an earthquake is time-dependent, controlled by viscous flow in the lower crust and upper mantle (*Freed et al.*, 2006, *Gratier et al.*, 2014, *Pollitz*, 2005, *Yu et al.*, 2003). Laboratory derived flow laws associated with aseismic creep suggest a power law rheology (*Kirby*, 1983), and we simplify the equation to directly relate the cumulative afterslip s and time t in the form (e.g. *Çakir et al.* (2012), *Gratier et al.* (2014)): $s = \alpha t^n$, where α and n are the power law parameters. The

power law exponent n was found to vary with rock type and grain size in laboratory experiments (*Gratier et al.*, 2014), and range from 0.25–0.5 in natural earthquakes (*Çakir et al.*, 2012, *Freed et al.*, 2006, *Gratier et al.*, 2014). Postseismic deformation on a fault may consist of different stages, as the effective viscosity varies as a function of time (*Freed et al.*, 2006). The viscosity after an earthquake will recover to pre-earthquake levels (after a few years to decades, e.g. ∼50 years (*Freed et al.*, 2006)). Hence, the variation in power law parameters provides information about the characteristic healing time of the fault (*Gratier et al.*, 2014).

In this study, we used the measurements of the postseismic afterslip following the 1978 earthquake to estimate the power law parameters. The 7 m slip in 1974-2013 involves both coseismic and postseismic motion, and we cannot separate these two periods directly due to a temporal lack of data coverage. The 1.5 m vertical displacement measured by *Berberian* (1979) provides a constraint for the coseismic slip on the Tabas fold (which is 30% of the total vertical motion), though note that the 1.5 m combines both 35 cm of primary slip, plus cumulative secondary bedding-plane slip. We estimated a maximum coseismic slip of 2.1 m (7 m×30%), and a minimum postseismic afterslip of ∼4.4 m in 1974–1991 and ∼0.5 m in 1991–2013. Also, note that the 1.5 m displacement could have all formed during the postseismic period in the 10 days before they were observed by *Berberian* (1979), in which case, none of the slip is coseismic. Therefore, the maximum postseismic afterslip would be ∼6.5 m in the time interval 1974–1991 (assuming no coseismic mo-

tion). We then calculated the power law parameters, α and n. Because the noise level of our measurements is high ($\sim$1/20 of the pixel size), and we do not have enough data to plot points throughout the postseismic period, particularly in the early postseismic period (1–5 years after the earthquake), all the fits (with exponents of 0.02–0.25) are possible (as shown in Figure 6). Combining the afterslip rate of 5$\pm$1 mm/yr between 1996 and 1999 (*Copley*, 2014) and assuming it is relatively accurate, the postseismic afterslip can be best-fitted with a power law exponent of $\sim$0.02. Our power law exponent, though not well constrained, appears to be smaller (by an order of a magnitude) than those observed in other natural earthquakes (the 1999 Izmit and 2004 Parkfield earthquakes), but the observations of those well-studied cases (e.g. (*Çakir et al.*, 2012, *Gratier et al.*, 2014)) cover a relatively early stage in the postseismic period compared with the 1978 Tabas earthquake. As discussed in *Freed et al.* (2006) and *Gratier et al.* (2014), the power law parameters vary with time. In the late stage of the postseismic period, the power law exponent should decrease to zero as the fault will be locked eventually (in the interseismic period). The small power law exponent observed in our study indicates a transition from the postseismic to interseismic periods.

5.3. Faulting in the Tabas region

Combining all our observations and the previous work on the Tabas earthquake, e.g. *Berberian* (1979, 1982), *Berberian et al.* (1979), *Copley* (2014), *Walker et al.* (2003, 2013), we propose a self-consistent model of faulting in

the Tabas region (Figure 7). Postseismic InSAR (*Copley*, 2014) and our image matching results suggest a high-angle ramp beneath the Tabas fold. It is worth noting that our modelling results show the main fault plane comes very close to the surface (∼0.1 km at depth), but did not reach the surface. We identified a ∼220 m wide zone of bedding plane slip on the surface (Figures 7a and 7b), which was reported to have ruptured in the 1978 earthquake (*Berberian*, 1979). We developed a conceptual model to reconcile the geodetic results and the geomorphological features, as illustrated in Figure 7c. The dip of the ramp (∼50°) starts to decrease at a depth of ∼0.1 km as it enters an upper layer of young, unconsolidated alluvial deposits (e.g. *Vallage et al.* 2015), and the amount of slip dissipates, such that only 35 cm was observed on the frontal east-dipping thrust in the month after the earthquake. The larger part of the coseismic slip instead reaches the surface through motion on a series of small high-angle thrust faults formed between underlying Neogene beds, which are related to distributed shearing in the immediate hanging wall. As slip diminishes towards the surface, folding increases, resulting in a narrow band of bedding slip faults in the immediate hanging wall to accommodate shearing (Figure 7c).

The Tabas fold is only one of two active structures at that latitude. *Berberian* (1979) also observed a high-angle (80°) reverse displacement along the Espakh fold, situated east of the Tabas fold (Figure 2), but we found no evidence for motion on the Espakh fold from image correlation. A cross-section (Figure 8) was constructed to show the geometry of faulting in this region.

The source parameters of the main shock indicate slip on a low-angle (16°) detachment fault with a centroid depth of 9 km with the epicentre under the Shotori Mountains (*Walker et al.*, 2003). Vertical displacements at the western margins of the Tabas and Espakh folds are the result of slip on associated ramps, which are connected by a flat at a depth of ∼5–6 km (Figure 8a). The flat shallows into the detachment that joins the Shotori range-front fault at a depth of ∼9 km (6 km + 12 km × tan 16°, Figure 8a). Given the fact that we do not have constraints on the subsurface structure of the Espakh fold, it is also possible that both ramps are connected by a planar detachment fault (dipping 16°) (Figure 8b), which would require that the Espakh fault reaches a depth of ∼7–9 km, and the Shotori range-front fault joins the detachment at a depth of ∼12 km (6 km + 20 km × tan 16°, Figure 8b).

5.4. Long-term surface folding: Characteristic slip behaviour

The SPOT-6 DEM also enables us to analyse the long-term surface folding. We identified two river terraces (a younger terrace T1 and an older one T2) associated with the growth of the Tabas fault. Figure 9 shows three topographic profiles, S1-S1′ along a modern river channel, S2-S2′ along the T1 surface, and S3-S3′ along the T2 surface. As the topography is dominated by a depositional slope of the alluvial surface, we removed a regional gradient from each profile, as shown in Figures 9c-9e. Note that because only a fragment of T2 is preserved, we extended S3-S3′ onto the T1 surface in order to calculate the regional surface slope. We chose river channel S1-

S1′ for analysis because (1) unlike the big rivers, where the relatively young alluvial fans (T1 and T2) have been washed away, fragments of T1 are seen here (Figures 9a) which indicates that the river is likely to preserve recent earthquake motion, and (2) walls and dams have been built across other rivers to suppress floods and may have also changed the sedimentation and erosion patterns since the earthquake. The other rivers in the area do not show visible warping for the reasons outlined above.

The uplift profiles (Figures 9c-9e) indicate that warping of the river channel and both terraces occurs over a distance of ∼6–7 km, similar to that expected from the modelled fault geometry. The modern river channel should record the slip due to the single 1978 earthquake (∼5 m vertical motion as seen from DEM differencing and our model), whereas T1 and T2 should record a cumulative fault slip from multiple earthquakes. We used the fault model from Section 5.1 to predict the uplift of the river channel and terraces. If the river channel only records the motion of the 1978 earthquakes, the uplift along profile S1-S1′ can be determined from the Okada model (*Okada*, 1985) with a fault slip of 7 m. As shown in Figure 9c, the modelled uplift is consistent with that measured (∼5.0 m).

To estimate the fault slip responsible for the uplift of river terraces T1 and T2, we fixed the fault geometry, i.e. a fault plane dipping 50° beneath depths of 0.1 km to 6 km at its base, and varied the slip from 11-23 m in steps of 1 m (as shown in Figure 9). To produce the uplift of T1 (∼9.5 m), a fault slip of 13–14 m is needed. The uplift of T2 (∼14 m) requires a fault

slip of 21–22 m. Note that profile S3-S3′ at the eastern end was drawn on the T1 surface, which causes underestimation of the uplift compared to that from the model. The inferred slip (13–14 m and 21–22 m) appears to be multiples of the slip in the 1978 earthquake (7 m), indicating that T1 and T2 possibly record two and three earthquakes, with a similar magnitude to the 1978 event. It is possible that the inferred slip was caused by more than three events with smaller magnitudes. If that was the case, we would expect to see more river terraces with smaller height changes. However, as we only observed two levels of river terrace, it is plausible that T1 and T2 simply record two and three repeated earthquakes respectively.

The good agreement between the modelled surface uplift and the measured folding suggests that the Tabas fold may exhibit characteristic slip behaviour. Such behaviour was also observed on the Hoshab fault in the eastern Makran from an investigation of the 2013 M_w 7.7 Balochistan earthquake (*Zhou et al.*, 2015a), and the Fuyun fault in China (*Klinger et al.*, 2011). As we do not have any direct measurements of the slip rate on the Tabas fault, we assume that the ∼1.5 mm/yr right-lateral strike-slip rate of the Nayband fault (*Foroutan et al.*, 2014, *Walker et al.*, 2009, 2013) is accommodated by repeated thrusting on the Tabas fold system (∼1 mm/yr in the shortening direction). Given an average of ∼3.5 m shortening, as observed in the 1978 earthquake, it would require a magnitude M_w 7.3 earthquake every ∼3,500 years. Future palaeoseismic studies are needed to confirm this. Nevertheless, we do not know the spatial extent of slip in the Tabas earth-

quake and hence the state of stress on neighbouring thrust faults. The 1978 Tabas earthquake could have brought neighbouring fault segments closer to failure. Better structure mapping and qualification of slip rates are required to better characterise the seismic hazard in this area.

6. Conclusions

Historical images have opened up new opportunities for studies of past earthquakes. In this study, we measured the horizontal motion associated with the 1978 M_w 7.3 Tabas earthquake using KH-9, SPOT-2 and SPOT-6 images, and the vertical motion using aerial photographs and SPOT-6 stereo imagery. The results are consistent and provide insights into the coseismic and long-lasting postseismic deformation. We found time-dependent shallow postseismic afterslip, decaying as αt^n with a best-fitting power law exponent of 0.02. Although we do not have any constraints on the afterslip in the early postseismic period, it is very likely that most of the afterslip occurred prior to 1991. From comparison of terrace heights with the earthquake uplift, we also found that the Tabas fold system may exhibit a characteristic slip behaviour. This behaviour requires a magnitude M_w 7.3 earthquake every $\sim$3500 years to accommodate the previously estimated shortening rate of $\sim$1.0 mm/yr. This study potentially provides a means to investigate palaeoseismology of the Tabas folds, despite a lack of obvious surface scarps. The method may be useful more generally in regions of fault-related folding.

Acknowledgements

This work was supported by the University of Oxford through a PAG scholarship to Yu Zhou, the National Natural Science Foundation of China (No. 41204027) to Xiaogang Song, and the Natural Environment Research Council through the Looking into the Continents from Space (LiCS) large grant (NE/K011006/1) and the Centre for the Observation and Modelling of Earthquakes, Volcanoes and Tectonics (COMET).

References

Astrium (2013), SPOT 6 & SPOT 7 Imagery User Guide, *Astrium GEO-Information Services, Toulouse, France*, p. 120.

Ayoub, F., S. Leprince, and L. Keene (2009), Users Guide to COSI-CORR Co-registration of Optically Sensed Images and Correlation, *California Institute of Technology: Pasadena, CA, USA*, p. 38.

Barišin, I., A. Hinojosa-Corona, and B. Parsons (2015), Co-seismic vertical displacements from a single post-seismic lidar DEM: example from the 2010 el Mayor-Cucapah earthquake, *Geophysical Journal International*, *202*(1), 328–346, doi:10.1093/gji/ggv139.

Berberian, M. (1979), Earthquake faulting and bedding thrust associated with the Tabas-e-Golshan (Iran) earthquake of September 16, 1978, *Bulletin of the Seismological Society of America*, *69*(6), 1861–1887.

549 Berberian, M. (1981), Active faulting and tectonics of Iran, *Zagros Hindu*
550 *Kush Himalaya Geodynamic Evolution*, pp. 33–69.

551 Berberian, M. (1982), Aftershock tectonics of the 1978 Tabas-e-Golshan
552 (Iran) earthquake sequence: a documented active 'thin-and thick-skinned
553 tectonic' case, *Geophysical Journal International*, *68*(2), 499–530.

554 Berberian, M., I. Asudeh, R. Bilham, C. Scholz, and C. Soufleris (1979),
555 Mechanism of the main shock and the aftershock study of the Tabas-e-
556 Golshan (Iran) earthquake of September 16, 1978: A preliminary report,
557 *Bulletin of the Seismological Society of America*, *69*(6), 1851–1859.

558 Brown, D. C. (1971), Close-range camera calibration, *Photogrammetric En-*
559 *gineering & Remote Sensing*, *37*, 855–866.

560 Burbank, D. W., and R. S. Anderson (2011), *Tectonic Geomorphology*, John
561 Wiley & Sons.

562 Burnett, M. G. (2012), Hexagon (KH-9)– Mapping camera program and
563 evolution, *National Reconnaissance Office (NRO), Center for the Study of*
564 *National Reconnaissance (CSNR), Chantilly, VA, USA*, p. 395.

565 Çakir, Z., S. Ergintav, H. Özener, U. Dogan, A. M. Akoglu, M. Meghraoui,
566 and R. Reilinger (2012), Onset of aseismic creep on major strike-slip faults,
567 *Geology*, *40*(12), 1115–1118.

568 Copley, A. (2014), Postseismic afterslip 30 years after the 1978 Tabas-e-
569 Golshan (Iran) earthquake: observations and implications for the geo-

570 logical evolution of thrust belts, *Geophysical Journal International*, doi:
571 10.1093/gji/ggu023.

572 Dolan, J. F., S. A. Christofferson, and J. H. Shaw (2003), Recognition of pa-
573 leoearthquakes on the Puente Hills blind thrust fault, California, *Science*,
574 *300*(5616), 115–118.

575 Elliott, J., R. Jolivet, P. González, J.-P. Avouac, J. Hollingsworth, M. Searle,
576 and V. Stevens (2016), Himalayan megathrust geometry and relation to
577 topography revealed by the Gorkha earthquake, *Nature Geoscience*.

578 England, P., and J. Jackson (2011), Uncharted seismic risk, *Nature Geo-*
579 *science*, *4*(6), 348–349.

580 Fattahi, M., R. Walker, M. Talebian, R. Sloan, and A. Rasheedi (2014), Late
581 Quaternary active faulting and landscape evolution in relation to the Gowk
582 Fault in the South Golbaf Basin, SE Iran, *Geomorphology*, *204*, 334–343,
583 doi:10.1016/j.geomorph.2013.08.017.

584 Feng, G., Z. Li, X. Shan, L. Zhang, G. Zhang, and J. Zhu (2015), Geodetic
585 model of the 2015 April 25 M_w 7.8 Gorkha Nepal Earthquake and M_w
586 7.3 aftershock estimated from InSAR and GPS data, *Geophysical Journal*
587 *International*, *203*(2), 896–900.

588 Fialko, Y., D. Sandwell, M. Simons, and P. Rosen (2005), Three-dimensional
589 deformation caused by the Bam, Iran, earthquake and the origin of shallow
590 slip deficit, *Nature*, *435*(7040), 295–299.

591 Foroutan, M., B. Meyer, M. Sébrier, H. Nazari, A. Murray, K. Le Dortz,
592 M. Shokri, M. Arnold, G. Aumaître, D. Bourlès, et al. (2014), Late
593 Pleistocene-Holocene right slip rate and paleoseismology of the Nayband
594 fault, western margin of the Lut block, Iran, *Journal of Geophysical Re-*
595 *search: Solid Earth*, *119*(4), 3517–3560, doi:10.1002/2013JB010746.

596 Freed, A. M., R. Bürgmann, E. Calais, and J. Freymueller (2006), Stress-
597 dependent power-law flow in the upper mantle following the 2002 Denali,
598 Alaska, earthquake, *Earth and Planetary Science Letters*, *252*(3), 481–489.

599 Funning, G. J., B. Parsons, T. J. Wright, J. A. Jackson, and E. J. Fielding
600 (2005), Surface displacements and source parameters of the 2003 Bam
601 (Iran) earthquake from Envisat advanced synthetic aperture radar imagery,
602 *Journal of Geophysical Research: Solid Earth*, *110*(B9).

603 Grandin, R., M. Vallée, C. Satriano, R. Lacassin, Y. Klinger, M. Simoes,
604 and L. Bollinger (2015), Rupture process of the M_w= 7.9 2015 Gorkha
605 earthquake (Nepal): insights into Himalayan megathrust segmentation,
606 *Geophysical Research Letters*, *42*(20), 8373–8382.

607 Gratier, J. P., F. Renard, and B. Vial (2014), Postseismic pressure solu-
608 tion creep: Evidence and time-dependent change from dynamic indenting
609 experiments, *Journal of Geophysical Research: Solid Earth*, *119*(4), 2764–
610 2779, doi:10.1002/2013JB010768.

611 Hessami, K. (2002), Tectonic history and present-day deformation in the
612 Zagros fold-thrust belt, *Acta Universitatis Upsaliensis*.

613 Hollingsworth, J., J. Jackson, R. Walker, and H. Nazari (2008), Extrusion
614 tectonics and subduction in the eastern South Caspian region since 10 Ma,
615 *Geology*, *36*(10), 763–766.

616 Hollingsworth, J., S. Leprince, F. Ayoub, and J.-P. Avouac (2012), Deforma-
617 tion during the 1975–1984 Krafla rifting crisis, NE Iceland, measured from
618 historical optical imagery, *Journal of Geophysical Research: Solid Earth*
619 *(1978–2012)*, *117*(B11), doi:10.1029/2012JB009140.

620 Hubbard, J., and J. H. Shaw (2009), Uplift of the Longmen Shan and Ti-
621 betan plateau, and the 2008 Wenchuan (M = 7.9) earthquake, *Nature*,
622 *458*(7235), 194–197.

623 Jackson, J. (2001), Living with earthquakes: know your faults, *Journal of*
624 *Earthquake Engineering*, *5*(spec01), 5–123.

625 Jackson, J., J. Haines, and W. Holt (1995), The accommodation of Arabia-
626 Eurasia plate convergence in Iran, *Journal of Geophysical Research: Solid*
627 *Earth (1978–2012)*, *100*(B8), 15,205–15,219.

628 Kirby, S. H. (1983), Rheology of the lithosphere, *Reviews of Geophysics*,
629 *21*(6), 1458–1487.

630 Klinger, Y., M. Etchebes, P. Tapponnier, and C. Narteau (2011), Character-

istic slip for five great earthquakes along the Fuyun fault in China, *Nature Geoscience*, *4*(6), 389–392.

Leprince, S., S. Barbot, F. Ayoub, and J.-P. Avouac (2007), Automatic and precise orthorectification, coregistration, and subpixel correlation of satellite images, application to ground deformation measurements, *Geoscience and Remote Sensing, IEEE Transactions on*, *45*(6), 1529–1558.

Meyer, B., and K. Le Dortz (2007), Strike-slip kinematics in central and eastern Iran: Estimating fault slip-rates averaged over the Holocene, *Tectonics*, *26*(5).

Mollberg, B., and B. Schardt (1988), Mission report on the Orbiter Camera Payload System (OCPS) Large Format Camera (LFC) and Attitude Reference System (ARS).

Molnar, P., and H. Lyon-Caen (1989), Fault plane solutions of earthquakes and active tectonics of the Tibetan Plateau and its margins, *Geophysical Journal International*, *99*(1), 123–153.

Molnar, P., T. J. Fitch, and F. T. Wu (1973), Fault plane solutions of shallow earthquakes and contemporary tectonics in Asia, *Earth and Planetary Science Letters*, *19*(2), 101–112.

Mousavi, Z., A. Walpersdorf, R. Walker, F. Tavakoli, E. Pathier, H. Nankali, F. Nilfouroushan, and Y. Djamour (2013), Global Positioning System con-

straints on the active tectonics of NE Iran and the South Caspian region, *Earth and Planetary Science Letters*, *377*, 287–298.

Okada, Y. (1985), Surface deformation due to shear and tensile faults in a half-space, *Bulletin of the Seismological Society of America*, *75*(4), 1135–1154.

Oskin, M. E., J. R. Arrowsmith, A. H. Corona, A. J. Elliott, J. M. Fletcher, E. J. Fielding, P. O. Gold, J. J. G. Garcia, K. W. Hudnut, J. Liu-Zeng, and O. J. Teran (2012), Near-field deformation from the El Mayor–Cucapah earthquake revealed by differential LIDAR, *Science*, *335*(6069), 702–705.

Pollitz, F. F. (2005), Transient rheology of the upper mantle beneath central Alaska inferred from the crustal velocity field following the 2002 Denali earthquake, *Journal of Geophysical Research: Solid Earth*, *110*(B8).

Regard, V., O. Bellier, R. Braucher, F. Gasse, D. Bourlès, J. Mercier, J.-C. Thomas, M. Abbassi, E. Shabanian, and S. Soleymani (2006), ^{10}Be dating of alluvial deposits from Southeastern Iran (the Hormoz Strait area), *Palaeogeography, Palaeoclimatology, Palaeoecology*, *242*(1), 36–53.

Scholz, C. H. (1982), Scaling laws for large earthquakes: consequences for physical models, *Bulletin of the Seismological Society of America*, *72*(1), 1–14.

Segall, P., R. Bürgmann, and M. Matthews (2000), Time-dependent triggered

671 afterslip following the 1989 Loma Prieta earthquake, *Journal of Geophys-*
672 *ical Research: Solid Earth (1978–2012)*, *105*(B3), 5615–5634.

673 Suito, H., and J. T. Freymueller (2009), A viscoelastic and afterslip post-
674 seismic deformation model for the 1964 Alaska earthquake, *Journal of*
675 *Geophysical Research: Solid Earth (1978–2012)*, *114*(B11).

676 Surazakov, A., and V. Aizen (2010), Positional accuracy evaluation of de-
677 classified Hexagon KH-9 mapping camera imagery, *Photogrammetric En-*
678 *gineering & Remote Sensing*, *76*(5), 603–608.

679 Tapponnier, P., B. Meyer, J. P. Avouac, G. Peltzer, Y. Gaudemer, G. Shun-
680 min, X. Hongfa, Y. Kelun, C. Zhitai, C. Shuahua, et al. (1990), Active
681 thrusting and folding in the Qilian Shan, and decoupling between upper
682 crust and mantle in northeastern Tibet, *Earth and Planetary Science Let-*
683 *ters*, *97*(3), 382–403.

684 Tatar, M., D. Hatzfeld, J. Martinod, A. Walpersdorf, M. Ghafori-Ashtiany,
685 and J. Chéry (2002), The present-day deformation of the central Zagros
686 from GPS measurements, *Geophysical Research Letters*, *29*(19), 33–1.

687 Vallage, A., Y. Klinger, R. Grandin, H. Bhat, and M. Pierrot-Deseilligny
688 (2015), Inelastic surface deformation during the 2013 M_w 7.7 Balochistan,
689 Pakistan, earthquake, *Geology*, *43*(12), 1079–1082.

690 Vernant, P., F. Nilforoushan, D. Hatzfeld, M. Abbassi, C. Vigny, F. Masson,
691 H. Nankali, J. Martinod, A. Ashtiani, R. Bayer, et al. (2004a), Present-day

crustal deformation and plate kinematics in the Middle East constrained by GPS measurements in Iran and northern Oman, *Geophysical Journal International*, *157*(1), 381–398.

Vernant, P., F. Nilforoushan, J. Chery, R. Bayer, Y. Djamour, F. Masson, H. Nankali, J.-F. Ritz, M. Sedighi, and F. Tavakoli (2004b), Deciphering oblique shortening of central Alborz in Iran using geodetic data, *Earth and planetary science letters*, *223*(1), 177–185.

Walker, R., and J. Jackson (2004), Active tectonics and late Cenozoic strain distribution in central and eastern Iran, *Tectonics*, *23*(5).

Walker, R., J. Jackson, and C. Baker (2003), Surface expression of thrust faulting in eastern Iran: source parameters and surface deformation of the 1978 Tabas and 1968 Ferdows earthquake sequences, *Geophysical Journal International*, *152*(3), 749–765.

Walker, R., P. Gans, M. Allen, J. Jackson, M. Khatib, N. Marsh, and M. Zarrinkoub (2009), Late Cenozoic volcanism and rates of active faulting in eastern Iran, *Geophysical Journal International*, *177*(2), 783–805.

Walker, R., M. Khatib, A. Bahroudi, A. Rodés, C. Schnabel, M. Fattahi, M. Talebian, and E. Bergman (2013), Co-seismic, geomorphic, and geologic fold growth associated with the 1978 Tabas-e-golshan earthquake fault in eastern Iran, *Geomorphology*, *237*, 98–118.

712 Walpersdorf, A., D. Hatzfeld, H. Nankali, F. Tavakoli, F. Nilforoushan,
713 M. Tatar, P. Vernant, J. Chéry, and F. Masson (2006), Difference in the
714 GPS deformation pattern of North and Central Zagros (Iran), *Geophysical*
715 *Journal International*, *167*(3), 1077–1088.

716 Walpersdorf, A., I. Manighetti, Z. Mousavi, F. Tavakoli, M. Vergnolle, A. Ja-
717 didi, D. Hatzfeld, A. Aghamohammadi, A. Bigot, Y. Djamour, et al.
718 (2014), Present-day kinematics and fault slip rates in eastern Iran, de-
719 rived from 11 years of GPS data, *Journal of Geophysical Research: Solid*
720 *Earth*, *119*(2), 1359–1383, doi:10.1002/2013JB010620.

721 Wang, K., and Y. Fialko (2015), Slip model of the 2015 M_w 7.8 Gorkha
722 (Nepal) earthquake from inversions of ALOS-2 and GPS data, *Geophysical*
723 *Research Letters*, *42*(18), 7452–7458.

724 Yu, S.-B., Y.-J. Hsu, L.-C. Kuo, H.-Y. Chen, and C.-C. Liu (2003), GPS mea-
725 surement of postseismic deformation following the 1999 Chi-Chi, Taiwan,
726 earthquake, *Journal of Geophysical Research: Solid Earth*, *108*(B11).

727 Zhang, P.-Z. (2013), Beware of slowly slipping faults, *Nature Geoscience*,
728 *6*(5), 323–324.

729 Zhou, Y., J. R. Elliott, B. Parsons, and R. T. Walker (2015a), The
730 2013 Balochistan earthquake: An extraordinary or completely ordi-
731 nary event?, *Geophysical Research Letters*, *42*(15), 6236–6243, doi:
732 10.1002/2015GL065096.

733 Zhou, Y., B. Parsons, J. R. Elliott, I. Barisin, and R. T. Walker (2015b),
734 Assessing the ability of Pleiades stereo imagery to determine height changes
735 in earthquakes: A case study for the El Mayor-Cucapah epicentral area,
736 *Journal of Geophysical Research: Solid Earth*, *120*(12), 8793–8808, doi:
737 10.1002/2015JB012358.

Table 1: Images used in this study.

	Pre-earthquake		**Post-earthquake**	
	KH-9	**Aerial**	**SPOT-2**	**SPOT-6**
Time	9th Mar, 1974	13th Aug, 1956	6th Sep, 1991	29th Dec, 2013
Type	Frame camera	Frame camera	Pushbroom	Pushbroom
Resolution (m)	6-9	1-3	10	1.5
Focal length (cm)	30.5	15.524		

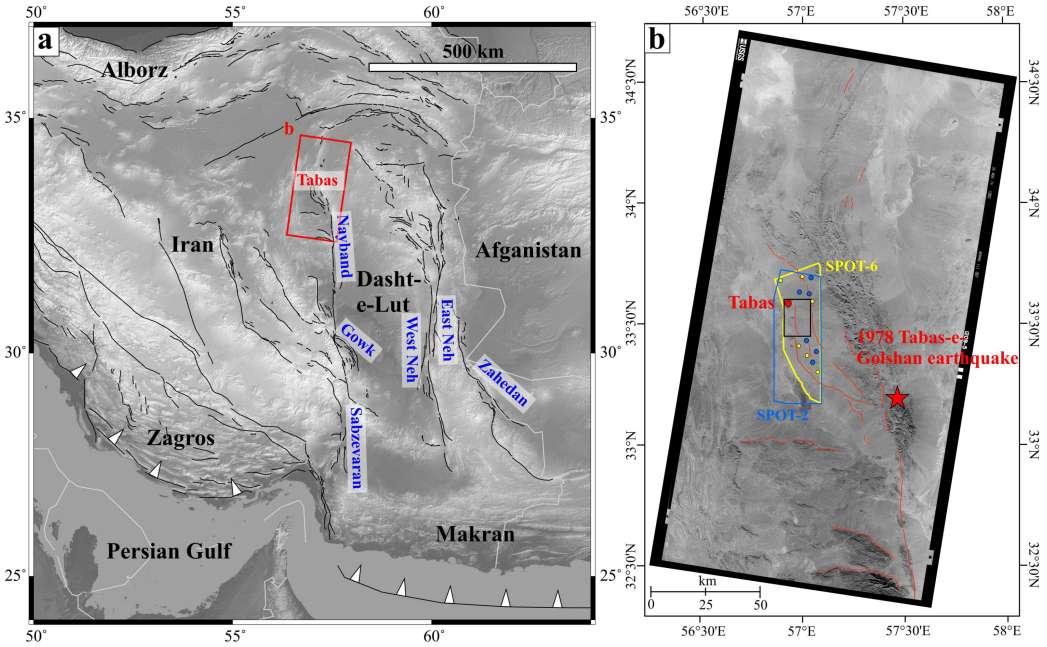

Figure 1: (a) Active faults (black lines) in Iran, from *Walker et al.* (2003). Red box shows the coverage of the pre-earthquake KH-9 image. (b) KH-9 image around the Tabas region. Red star indicates the epicentre of the 16 September, 1978 Tabas-e-Golshan earthquake, from *Walker et al.* (2003). Red lines are active faults. Red dot indicates the location of Tabas. Yellow polygon shows SPOT-6 stereo image coverage (Figure 2b). Yellow circles show the location of the GCPs used to co-register the KH-9 and SPOT-6 images. Blue polygon shows the SPOT-2 image coverage that we purchased for this study, with blue circles indicating the GCPs used to co-register the SPOT-2 and SPOT-6 images. Black box shows the area of Figure 3a.

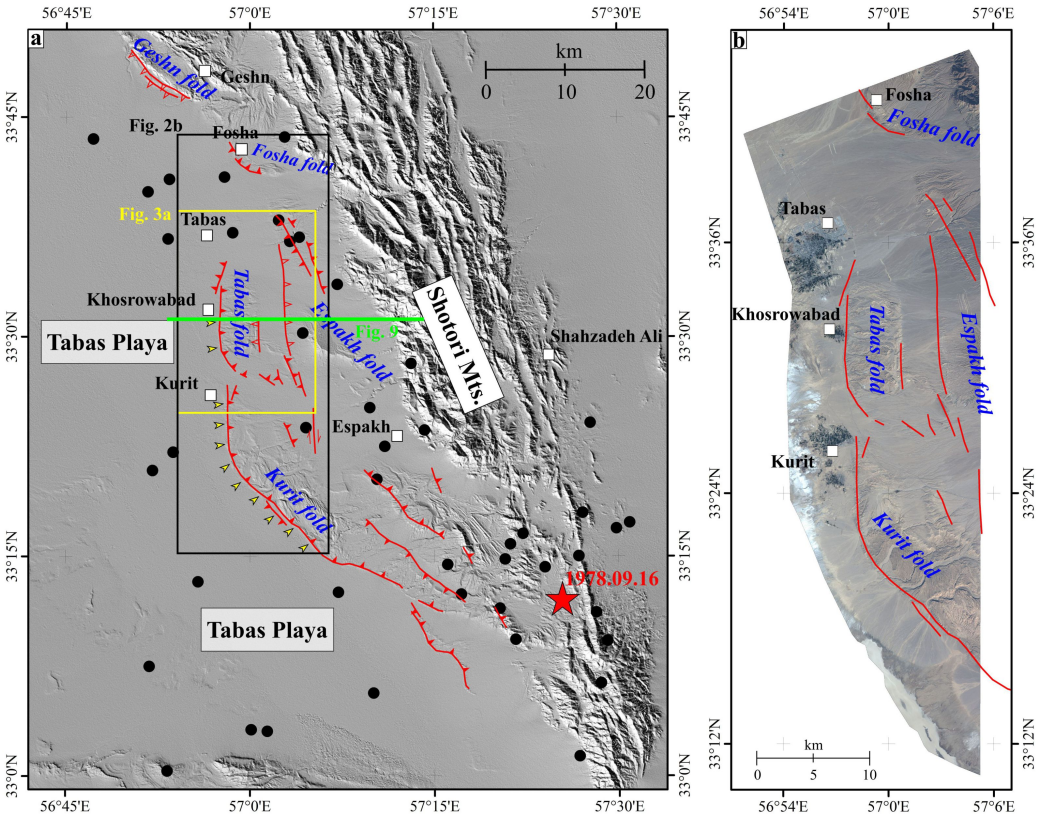

Figure 2: (a) Surface ruptures (red lines) observed in the field by *Berberian* (1979). Red filled triangles denote thrust faulting and open triangles are high-angle reverse faulting. Yellow arrows mark the segments that show afterslip in *Copley* (2014). Black dots are the epicentres of smaller earthquakes, from *Walker et al.* (2013). Green line shows the location of the topographic profile in Figure 8. (b) SPOT-6 orthoimagery showing the epicentral area of the 1978 Tabas earthquake. See (a) for location.

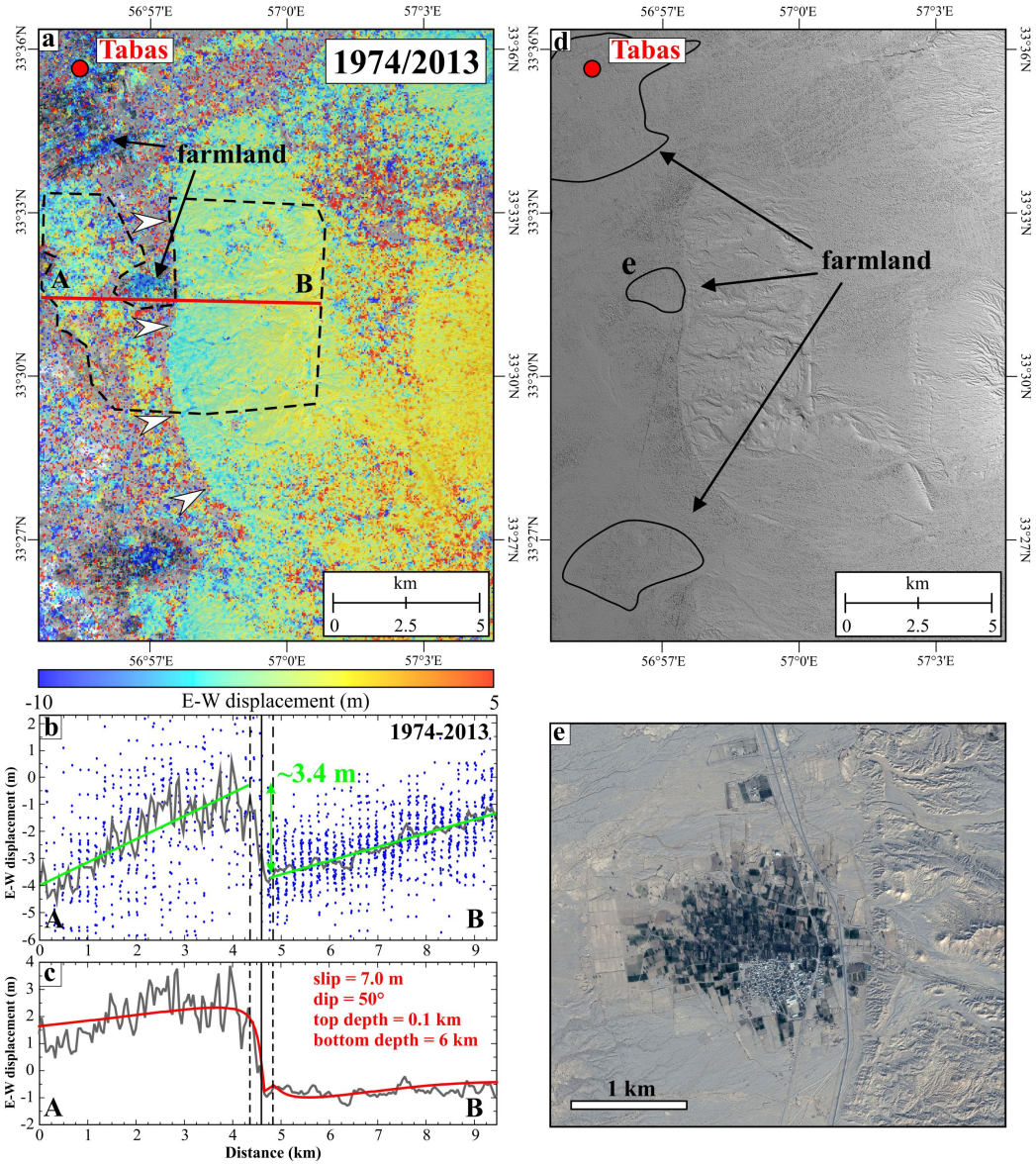

Figure 3: E-W displacement from correlating the KH-9 and SPOT-6 images. See Figure 2 for location. (a) E-W displacement map. White arrows indicate the deformation front. We projected the measurements included in the dashed polygon onto line AB and took the average in 50 m wide along-profile bins to estimate the displacement (i.e. shortening). Large deformation signals (blue areas) in the Tabas playa are due to farming. Red circle indicates Tabas. (b) Profile AB (gray line) shows a 3.4 m E-W displacement across the fold estimated by fitting two lines (green lines) on each side of the fault. Blue dots show the raw data points in (a). The measurements in the footwall are more scattered due to decorrelation of some pixels within the swath (white noise), and averaging cannot reduce these noises. (c) Displacements predicted with the Okada model of uniform slip on a rectangular fault plane. The best-fitting model through grid search (red line) is 7 m slip on a fault, dipping 50° beneath depths of 0.1 km to 6 km at its base. The model agrees very well with our measurement in the hanging wall, whereas the slightly larger misfit in the footwall is caused by decorrelation (white noise). (d) Shaded-relief SPOT-6 DEM showing the same region as (a). (e) SPOT-6 imagery showing farmland.

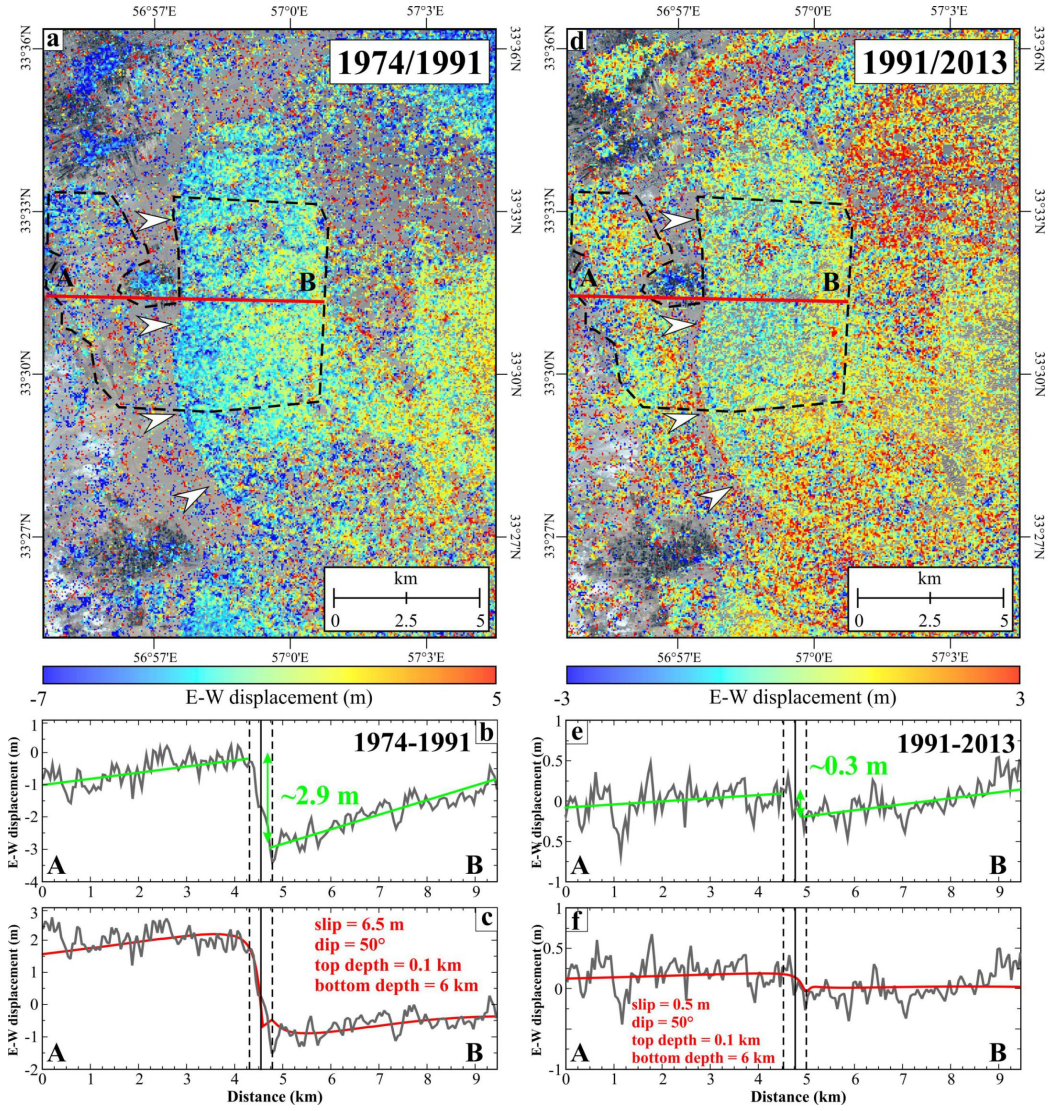

Figure 4: (a)–(c) As for Figure 3, but using the KH-9 and SPOT-2 images. Profile AB shows a 2.9±0.2 m E-W displacement. We fixed the fault geometry and varied the slip to reproduce this displacement. The best-fitting model gives a slip of 6.5 m. (d)–(f) As for Figure 3, but using the SPOT-2 and SPOT-6 images. Profile AB shows a 0.3±0.1 m E-W displacement. We fixed the fault geometry and varied the slip to reproduce this displacement. The best-fitting model gives a slip of 0.5 m.

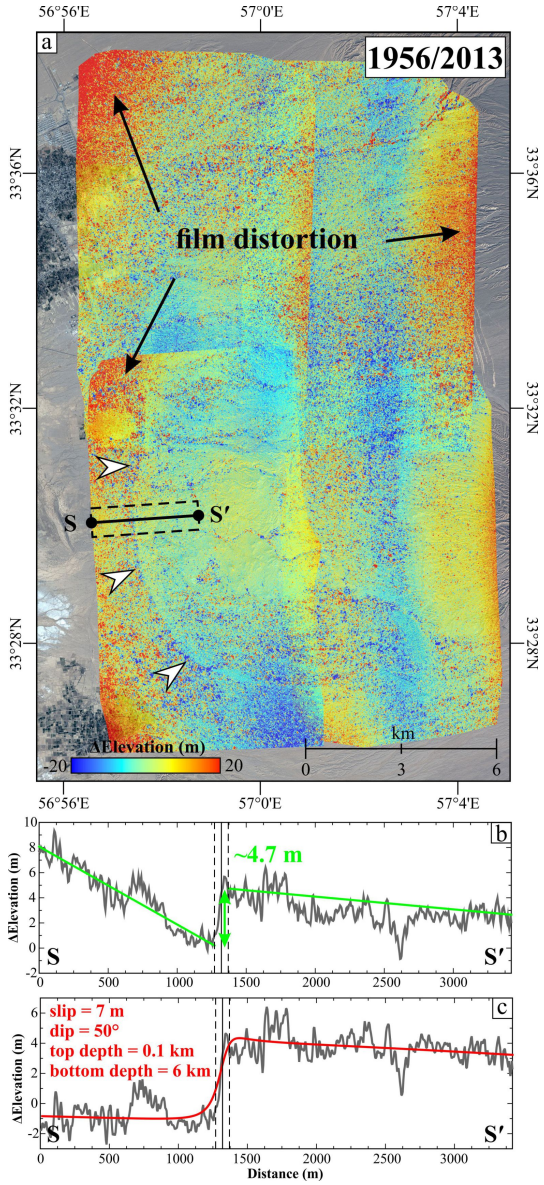

Figure 5: Height changes from direct differencing of the pre-earthquake aerial DEM and the post-earthquake SPOT-6 DEM. (a) Height change map. White arrows indicate the deformation front. We projected the measurements included in the polygon onto line SS′ and took the average in along-profile bins to estimate the displacement. (b) Profile SS′ shows a 4.7 m height change (gray line) estimated by fitting two lines (green lines) on each side of the fault. (c) Height changes predicted with the Okada model of 7 m slip on a rectangular fault plane, dipping 50° beneath depths of of 0.1 km to 6 km at its base. A third-order polynomial was fitted based on the residuals between the predicted displacement and the measured profile, and then removed to compensate for the film distortions. The prediction (red line) agrees well with our estimate.

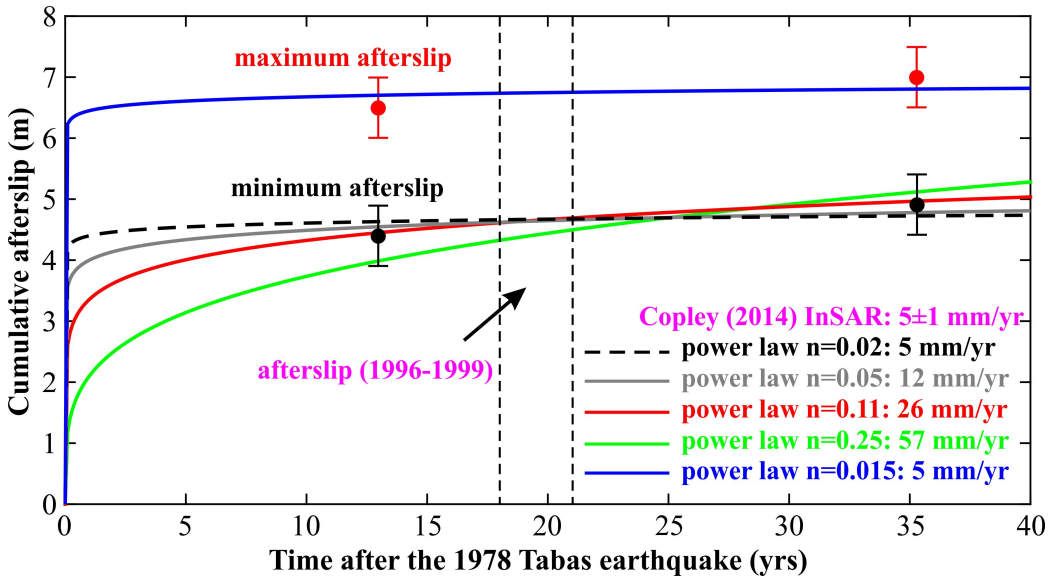

Figure 6: Time dependent postseismic afterslip and power law fits for the 1978 Tabas earthquake. We used $s = \alpha t^n$, where s is the cumulative afterslip, t is the time after the earthquake, and α and n (power law exponent) are the power law parameters that are related to fault healing. Black and red dots are measurements from image correlation (with an assumed error of $\sim 1/20 \times 10$ m=0.5 m). The maximum coseismic slip was estimated to be $\sim$2.1 m, leaving a minimum postseismic slip (black dots) of 4.4 m in 1978-1991 and 4.9 m in 1978-2013. The maximum postseismic slip (red dots) would be 6.5 m in the time interval 1978-1991, and 7.0 m in 1978-2013, assuming no coseismic motion. It is difficult to distinguish between different exponents in the range of 0.02–0.25 due to the noise level of our measurements and a lack of data in the early stage (0–5 years in particular). Dashed lines indicate an afterslip of 0.015 m (5 mm/yr$\times$3 years) in 1996-1999 estimated by *Copley* (2014), which was used as a constraint for determining the power law parameters. Combining the InSAR estimate and assuming it is very accurate, the postseismic afterslip can be best-fitted with a power law exponent of $\sim$0.02.

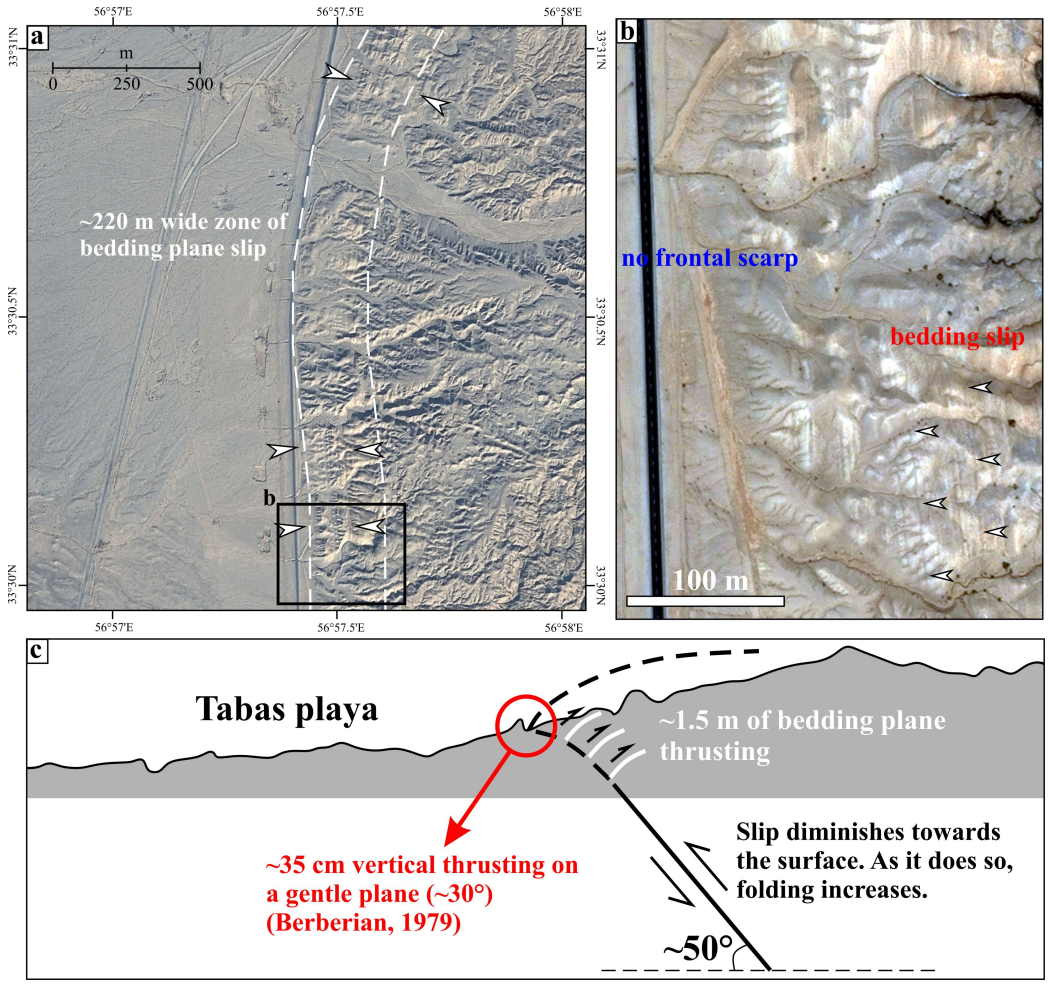

Figure 7: Schematic cross-section along the Tabas fold summarising the sub-surface structure. (a) SPOT-6 image showing a ∼220 m wide zone of bedding plane slip (indicated by white dashed lines). (b) A close-up view (from Bing Maps, http://www.bing.com/mapspreview) of bedding plane slip. We did not find any frontal scarps from the imagery. (c) Cartoon illustrating the sub-surface fault structure. The dip of main fault decreases at a depth of ∼0.1 km. *Berberian* (1979) found vertical displacement on a 30° dipping plane at surface. Most of the coseismic slip on the main fault reached the surface in the form of minor slip on a series of small thrust faults (white lines) developed between beds. As slip diminishes towards the surface, folding increases.

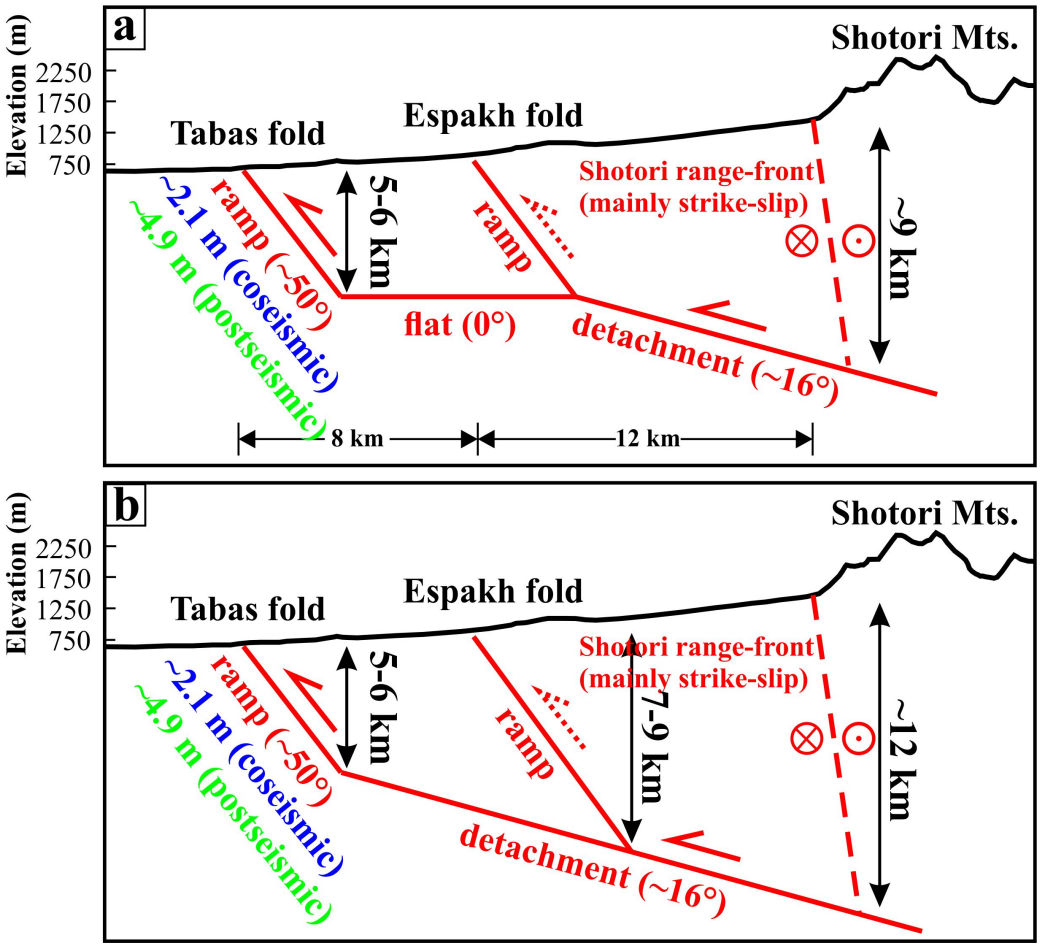

Figure 8: Schematic cross-section of faults in the Tabas region. See Figure 2 for location. As the subsurface structure of the Espakh fold is not well constrained by the uplift of the river terrace only, we show two possible scenarios of faulting in the region. (a) The Tabas and Espakh folds are connected by a flat at a depth of ∼5–6 km. The flat shallows into the detachment (dipping at ∼16° from *Walker et al.* (2003)), which joins the Shotori range-front fault at a depth of ∼9 km (6 km + 12 km × tan 16°). Vertical displacements across the Tabas fold measured by *Berberian* (1979) indicate that the coseismic slip on the Tabas ramp accounts for ∼30% of the total slip. Therefore, we speculated the coseismic slip on the fault plane is ∼2.1 m, with a postseismic afterslip of ∼4.9 m. (b) As for (a), but the Tabas and Espakh folds are connected by the detachment (dipping at ∼16°). This scenario requires the Espakh reaches a depth of 7–9 km, and the Shotori range-front fault joins the detachment at a depth of ∼12 km (6 km + 20 km × tan 16°).

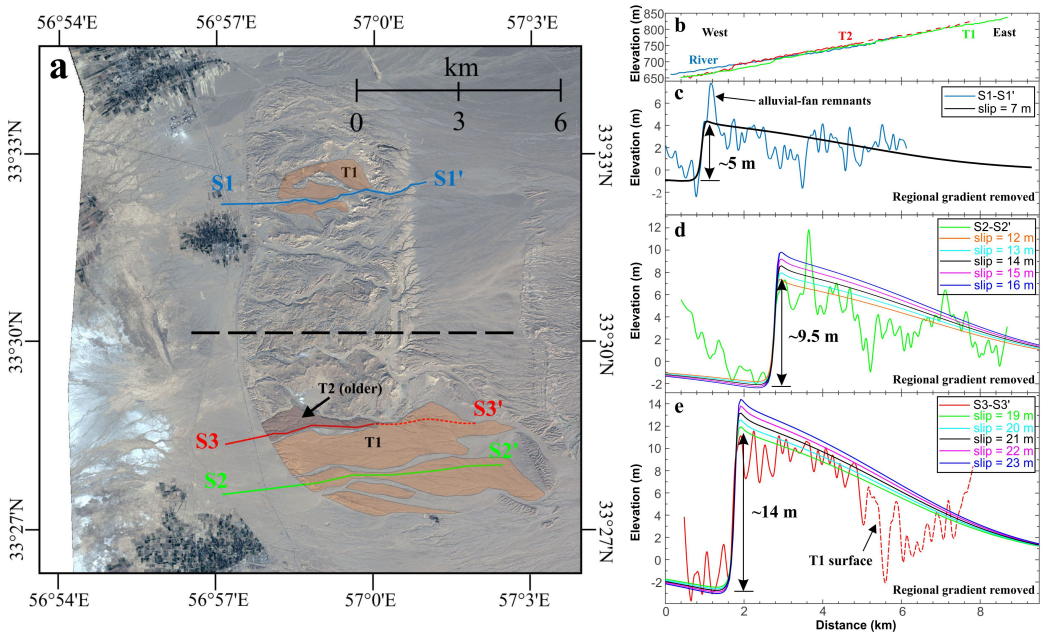

Figure 9: Long-term surface folding of the Tabas fold. (a) SPOT-6 orthoimage showing the Tabas fold. We identified two river terraces (T1 and T2) from the image and the DEM derived from it. Topographic profiles S1-S1′ (along a modern river channel), S2-S2′ (along the T1 surface), and S3-S3′ (along the T2 surface) were projected onto the fault-perpendicular direction (black dashed line). (b) Original topographic profiles from the SPOT-6 DEM. Blue, green and red lines indicate S1-S1′, S2-S2′ and S3-S3′ respectively. (c) Topographic profile S1-S1′ after removing a regional gradient. The black line is the predicted topography using the Okada model (*Okada*, 1985) and our estimated fault parameters (7 m slip on a 50° dipping fault, from a depth of 0.1 km to 6 km at its base). (d) Topographic profile S2-S2′ after removing a regional gradient. The predicted topography assume a model with a uniform slip (12–16 m in steps of 1 m) on a 50° dipping fault, from a depth of 0.1 km to 6 km at its base. (e) Topographic profile S3-S3′ after removing a regional gradient. The predicted topography assume a model of a uniform slip (19–23 m in steps of 1 m) on a 50° dipping fault, from a depth of 0.1 km to 6 km at its base.